

Filterless Visible-Range Color Sensing and Wavelength-Selective Photodetection Based on Barium/Nickel Codoped Bandgap-Engineered Potassium Sodium Niobate Ferroelectric Ceramics

Vasili A. Balanov, Filipp Temerov, Vladimir Pankratov, Wei Cao, and Yang Bai*

Photosensors, photodetectors, or color sensors are key components for various optical and optoelectronic applications. Semiconductor-based photodetection has been a dominator which is excellent at measuring the photon intensity of incident light. However, the wavelength of the incident light to be measured must be known beforehand and it mostly depends on auxiliary methods to filter unknown wavelengths. Herein, an alternative but simple mechanism that is using a monolithic, bandgap-engineered photoferroelectric ceramic to blindly determine the wavelength and intensity of incident light at the same time is demonstrated. The photoferroelectric compound is Ba- and Ni-codoped (K,Na) NbO_3 exhibiting a direct bandgap of ≈ 2 eV and a spontaneous polarization of ≈ 0.25 C m^{-2} . The band–band charge carrier transition is confirmed by multiple characterization methods of photoluminescence, photodielectric spectroscopy, and photoconductivity. The existent optoelectrical cumulative effect enabled by the simultaneous narrow bandgap and strong ferroelectricity allows to reliably distinguish the wavelengths of 405, 552, and 660 nm as well as the power density ranging from ≈ 0.1 to 10 W cm^{-2} , with the photoresponsivity of up to 60 $\mu\text{A W}^{-1}$. Consequently, this work proposes an alternative to semiconductor-based counterparts for filterless, wavelength-selective photodetection and color sensing.

systems for Internet of Things (IoT), and visible light communication.^[1–3] Since the 1960s, semiconductors like the conventional Si-based compounds, as well as the recently developed perovskites and low-dimensional options, have been dominating the materials used in photodetectors.^[4,5] The working mechanism relies on the separation and extraction of electron–hole pairs generated upon the absorption of incident photon energy higher than the bandgaps, when subject to bias electric field. As a result, the output electric signal (usually current under bias) is proportional to the irradiation intensity, thus providing the capability of sensing the intensity of the incident light.


However, semiconductor-based photodetectors do not always allow blind determination of the wavelength of the incident light. Instead, the wavelength needs to be defined or identified via auxiliary means, for example, photofilters from which the transmission spectrum is known in advance, before measuring the light intensity.^[6] The recent development of graphene-based, 2D, and halide perovskite

photodetectors has not made much difference in terms of the dependency on applying filters or tuning the compositions of the compounds for wavelength-selective photodetection.^[7–10] Therefore, filterless, wavelength-selective photodetection that can be realized on a monolithic material or single component

1. Introduction

Photodetectors, or photosensors in general, are the core components of many optical and optoelectronic applications such as photosensitive matrices in cameras, smart light-sensing

V. A. Balanov, Y. Bai
Microelectronics Research Unit
Faculty of Information Technology and Electrical Engineering
University of Oulu
FI-90570 Oulu, Finland
E-mail: yang.bai@oulu.fi

 The ORCID identification number(s) for the author(s) of this article can be found under <https://doi.org/10.1002/solr.202200995>.

© 2022 The Authors. Solar RRL published by Wiley-VCH GmbH. This is an open access article under the terms of the Creative Commons Attribution License, which permits use, distribution and reproduction in any medium, provided the original work is properly cited.

DOI: 10.1002/solr.202200995

F. Temerov, W. Cao
Nano and Molecular Systems Research Unit
Faculty of Science
University of Oulu
FI-90570 Oulu, Finland

V. Pankratov
Institute of Solid State Physics
University of Latvia
LV-1063 Riga, Latvia

capable of blindly telling the wavelength of the incident light is of great interest.^[9]

Compared to semiconductors, noncentrosymmetric materials with extremely low intrinsic conductivity, that is, ferroelectrics, can be promising candidates for wavelength-selective photodetection. Although electrons are barely mobile in the dark, the spontaneous polarizations in ferroelectrics may stimulate the separation and transportation of photogenerated electron–hole pairs, hence giving vastly different electric outputs when subject to different photon energies, especially to those higher than the bandgaps.^[11,12] It is proven that the electrical properties, including conductivity and photoinduced/stimulated polarization switching, will drastically change when both incident light with above-gap photon energy and an external electric field are applied simultaneously, known as the optoelectrical (or photoferroelectric) cumulative effect, compared to the cases where only individual light or electric field is present.^[13–15] This forms the fundamental basis of using “bandgap-engineered ferroelectrics” to distinguish the wavelength via the application of proper electric bias, given the fact that most ferroelectrics have bandgaps wider than 2.7 eV which is beyond the photon energy of most visible light and hence are not suitable for visible-range photodetection.^[16,17]

This work demonstrates the filterless, wavelength-selective photodetection using a bandgap-engineered ferroelectric ceramic made from the oxide perovskite compound of Ba- and Ni-codoped (K,Na)NbO₃. The bandgap of the material is defined via photoluminescence (PL) and the electrical properties are characterized by photodielectric and conductivity measurements. A photodetector device is fabricated for the demonstration purpose and the photoresponsivity is then examined. This is the first work presenting the functionality of bandgap-engineered ferroelectrics for filterless, wavelength-selective photodetection and thus paves a way toward robust, cost-effective, and energy-efficient photodetectors, photosensors, or color sensors with simple device configurations.

2. Physical Properties of the Studied Materials

The rationale of studying the specific composition in this work is that the family of Ba- and Ni-codoped (K,Na)NbO₃ (referred to as KNBNO, KNN-BNN, or KNN-BNNO) has been systematically and thoroughly optimized from several chemical and physical aspects in our previous works.^[13–15,18–27] Thus, it is much better known than other bandgap-engineered counterparts. In brief, two approaches could achieve to reduce the bandgap and retain reasonable ferroelectricity of the widely researched parental composition, (K,Na)NbO₃, simultaneously. One is to form a pure perovskite phase where the same proper amount of Ni²⁺ dopant and oxygen vacancy coexists.^[25] This is not easy in practice and will usually ruin either the ferroelectricity or bandgap

reduction.^[20] The other approach is picked up in this work where a proper amount of A-site vacancies have been designed in the raw mixture of reactants upon Ba and Ni doping. The A-site vacancy will naturally force the ceramic to grow into perovskite phase as well as tungsten bronze phase. Although tungsten bronze phase is considered detrimental in some piezoelectrics and ferroelectrics, it is not the case here. When the ratio between the two phases reaches the optimum (as indicated in **Table 1**), the bandgap value could be minimized and the retention of ferroelectricity maximized. The scientific reason behind is that the perovskite and tungsten bronze phases constructed a pseudomorphotropic phase boundary (MPB). It works in an analogical manner to the conventional MPB but instead of being in a frustration of two potential ferroelectric phases, the pseudo-MPB exists between ferroelectric perovskite phase and a polar tungsten bronze phase. In the intergranular interface, the pseudo-MPB bends the band structures in both the phases and thus reduces the bandgap. The frustration between the ferroelectric perovskite and polar tungsten bronze phases also eases domain wall motion and thus optimizes the ferroelectricity. Details can be found in literature and such an approach is easier to achieve in practice.^[18] The chemical and physical certainty provided by this approach sets the foundation of this work to understand its photodetection behavior.

Figure S1, Supporting Information, shows the results of X-ray diffraction (XRD), spectrophotometry, microscopy, and ferroelectric evaluation. The samples contained a major orthorhombic perovskite phase and a minor tetragonal tungsten bronze phase due to the intentionally introduced A-site deficiency (Figure S1a, Supporting Information, Table 1). Figure S2, Supporting Information, confirms the presence of the secondary phase where camel hump-like inclusions with an average height of 18 ± 5 nm, out of the generally homogenous major phase with nm-level roughness, could be clearly observed in the atomic force microscopy (AFM) graphs. The adjacent regions between the two phases naturally formed a heterojunction which reduced the pristine bandgap of >3–4 eV to ≈2 eV.^[14,18] Evidence of the bandgap reduction can be found in Figure S1b, Supporting Information, where the absorbance sharply increased between the incident photon energy of 1–3 eV while a direct band–band transition at ≈2.2 eV could be identified via the Tauc plot according to the $(F(R)-h\nu)^2$ curve ($F(R) = (1-R)^2/2R$, R is reflectance).

It is known that for complex, inhomogeneous, and polycrystalline samples, as is the case in this work (Figure S1a,c, Supporting Information, Table 1), the spectrophotometry and the Tauc method are no longer reliable for the determination of bandgaps.^[19] Therefore, to further confirm the bandgap and study the photoresponse, PL spectroscopy is employed with the specifications of the temperature-dependent PL (TDPL) and time-resolved PL (TRPL). The former is considered one of the

Table 1. Summary of nominal chemical formulas and phases of the mixture of reactants and the sintered ceramics.

Material	Nominal chemical formula	Phase	Concentration [mol.%]
Mixture of reactants	(K _{0.45 ± 0.01} Na _{0.37 ± 0.02} Ba _{0.05 ± 0.005})(Nb _{0.98 ± 0.001} Ni _{0.02 ± 0.001})O _{2.93 ± 0.01}	Miscellaneous	100
Sintered ceramics	(K _{0.54 ± 0.02} Na _{0.37 ± 0.02} Ba _{0.03 ± 0.005})(Nb _{0.996 ± 0.001} Ni _{0.004 ± 0.001})O _{2.98 ± 0.01}	Orthorhombic perovskite	83 ± 8
	(K _{0.25 ± 0.02} Na _{0.10 ± 0.01} Ba _{0.19 ± 0.01})(Nb _{0.97 ± 0.005} Ni _{0.03 ± 0.005})O _{2.82 ± 0.01}	Tetragonal tungsten bronze	17 ± 8

most powerful optical characterization methods for determination of carrier transport and localized states in semiconductor materials, the luminescence of impurities, and point defects.^[28–31] The latter probes the possible charge migrations next to the luminescent centers, yet, giving the possible charge transfer between the heterojunctional counterparts.^[32]

Figure 1 shows the results of the PL spectroscopy. In Figure 1a, the TDPL spectra of the samples were measured in the temperature range of 10–160 K and in the wavelength range of 450–700 nm. The PL intensity was the strongest at the lowest temperature (10 K) and decreased gradually with the temperature increase of up to 160 K, showing the maximum at ≈ 585 nm. The PL peak increased as the temperature decreased, implying that electrons in the valence band were being transferred into the conduction band and then being further relaxed back to the valence band in a radiative manner (radiative recombination) at lower temperature. This type of radiative recombination is fluorescence, as other peaks (intersystem electron transition) were not reordered.^[33] However, the thermomotion of electrons became predominant at high temperature and weakened the radiative decay.

The observed bandgap from the PL was likely to be about 2.12 eV (585 nm at 10 K), in agreement with the results of the spectrophotometry (UV–vis–NIR) (Figure S1b, Supporting Information and previous work).^[18] The observed bandgap could be considered a direct band–band transition since direct-bandgap semiconductors usually show dominant direct-gap recombination at low temperatures while, at higher temperatures, the direct-gap PL redshifts and the intensity decreases.^[34] It is important to note that the bandgap value from the PL data varies significantly since the PL spectra depend on multiple factors including crystalline defects, impurities, dopants, and contribution of the nonradiative energy transfer.^[35] In this work, the

evidence and ground for a direct-bandgap consideration is that, if a relaxing electron would release its energy as a phonon and then as a photon, another peak would have appeared, that is, a phosphorescence process.^[36]

To study the TRPL decay dynamics, TRPL spectra with a temperature interval of 10 K were measured as shown in Figure 1b. The curves were fit by a biexponential decay function in Equation (1).

$$f(t) = A_1 e^{-t/t_1} + A_2 e^{-t/t_2} \quad (1)$$

where t_1 and t_2 are the times of the fast and slow decay components, and A_1 and A_2 correspond to the weights of the fast and slow decay components, respectively. The fast decay process originates from the direct recombination of excitations, and the slow decay process derives from exciton recombination that is affected by exciton–phonon interaction. The direct or indirect recombination of excitons belongs to the radiation recombination process, where PL radiation can be observed in this process.^[37] As summarized in Figure 1c, at low temperatures (< 50 K), the decay curves had two components. The slow component started to vanish when the temperature increased due to the predominance of the nonradiative recombination process over radiative recombination and/or electron transfer between crystalline phases.^[38,39] Further elevation of temperature (> 85 – 95 K) led to a complete disappearing of the slow component and only the fast component could be observed. Notably, the relaxation time decreased with the increase of temperature.

The maxima of the excitation spectrum were registered at 356, 384, and 410 nm while the emission wavelength was set at 600 nm, as shown in Figure 1d. It is considered that the emission and excitation spectra for certain materials are mirror images of each other and the emission spectrum occurs at lower energy

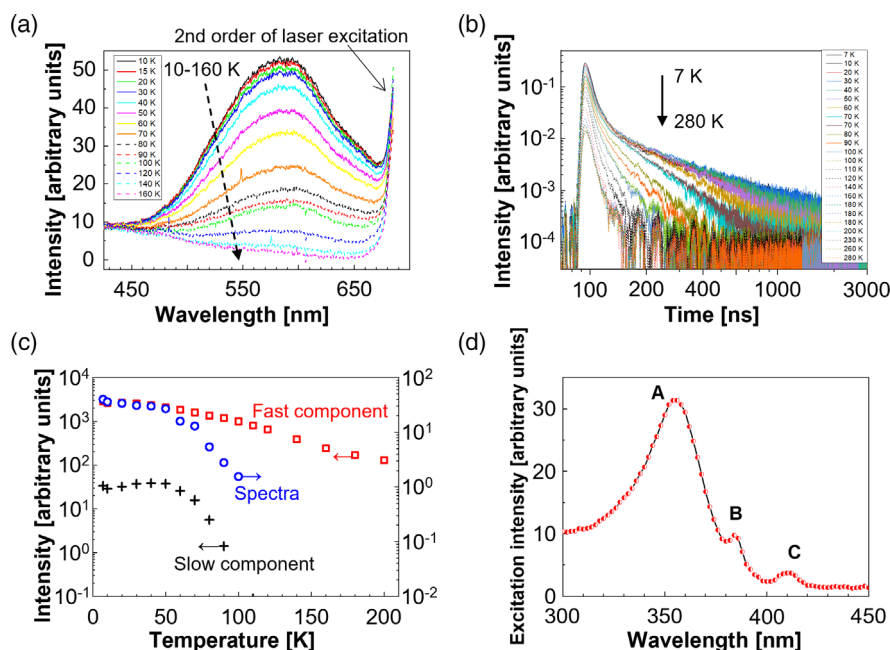


Figure 1. PL responses: a) The temperature dependence of the PL spectra and b) decay kinetics of the 600 nm emission, under 350 nm laser excitation. c) Summary of the temperature evolutions of the luminescence spectra intensities (blue circles) and the intensities of the fast (red squares) and slow (black crosses) components of the decay kinetics. d) The excitation spectrum of the 600 nm emission.

(higher wavelengths).^[40] In this work, both the emission and excitation spectra fit theory well, revealing the major peak at 356 nm.

3. Photodielectric Behavior

In order to further understand the influence of the bandgap on electrical and optoelectrical properties, **Figure 2** compares the normalized dielectric properties under different illumination conditions as well as for different poling statuses. Figure S3, Supporting Information, provides corresponding data for the measured values (before normalization). Measurement of dielectric properties with an LCR meter reveals evidence of the features of conductivity. The measured permittivity (ϵ) comprises the real permittivity of the material (ϵ') and the imaginary component contributed by the dielectric loss (ϵ''), that is, $\epsilon = \epsilon' + i\epsilon''$. In particular, a well-insulating dielectric material usually shows a relatively high ϵ (e.g., $>10^2$) and low ϵ'' (e.g., $<10^{-1}$). When the contribution of the polarization switching (domain reorientation) increases, as is the case of ferroelectric materials with randomly oriented domains, ϵ'' moderately increases (e.g., to $<10^{-1}$). In this scenario, the change of ϵ does not necessarily follow the change of ϵ'' since ϵ' is dominant and is determined by the intrinsic material properties and microstructure (e.g., grain sizes, densification level, etc.). For both the above cases, ϵ is considered close to ϵ' since ϵ'' is negligible. In principle, when the domains are aligned, for example, for poled ferroelectrics, the trend of ϵ'' should become less chaotic while freely mobile charge carriers in the material become more influential when given the similar intrinsic material properties and microstructure. In this case, the change of ϵ is likely to follow

the change of ϵ'' when the concentration of free charge carriers cannot be ignored.

As shown in Figure 2a, the measured relative permittivity (ϵ_r) of the unpoled status increased with the decrease of the incident light wavelength for 552 nm (photon energy 2.25 eV) and 405 nm (3.06 eV) at frequencies lower than 200 kHz. The ϵ_r under the 405 nm light dropped below the dark level while that under the 552 nm light remained above the dark level. However, the dielectric loss factor ($\tan \delta$) values in Figure 2c decreased at <100 Hz when the sample was illuminated. At 100 Hz–200 kHz, the trend of $\tan \delta$ was in line with ϵ_r (Figure 2a) for 552 and 405 nm. At >200 kHz, the $\tan \delta$ for 552 nm went slightly below the dark level while that for 405 nm remained above the dark level. When illuminated by the 660 nm light (1.88 eV), both the ϵ_r and $\tan \delta$ values were smaller than the corresponding dark values at <2 kHz (Figure 2a,c). At >2 kHz, the $\tan \delta$ remained below the dark level but ϵ_r became larger than the dark level. In other words, the evolution of photodielectric properties for the unpoled status was chaotic and no clear trend could be observed.

Such a chaos could be explained by the fact that incident light, regardless of the photon energy being above or below the bandgap of the material, is able to reorient ferroelectric domains.^[15,26,41,42] The photoexcited/stimulated domain wall motion made the ϵ_r values in Figure 2a to be predominantly affected by the domain reorientation, wherein to what extent was hard to predict under different illuminations for such a polycrystalline, multidomain material and hence resulting in no visible trend.

On the contrary, the trend of ϵ_r and $\tan \delta$ for the poled status was clear. In the full measurement range (20 Hz–1 MHz), ϵ_r increased with the decrease of the incident light wavelength (or with the increase of the incident light photon energy)

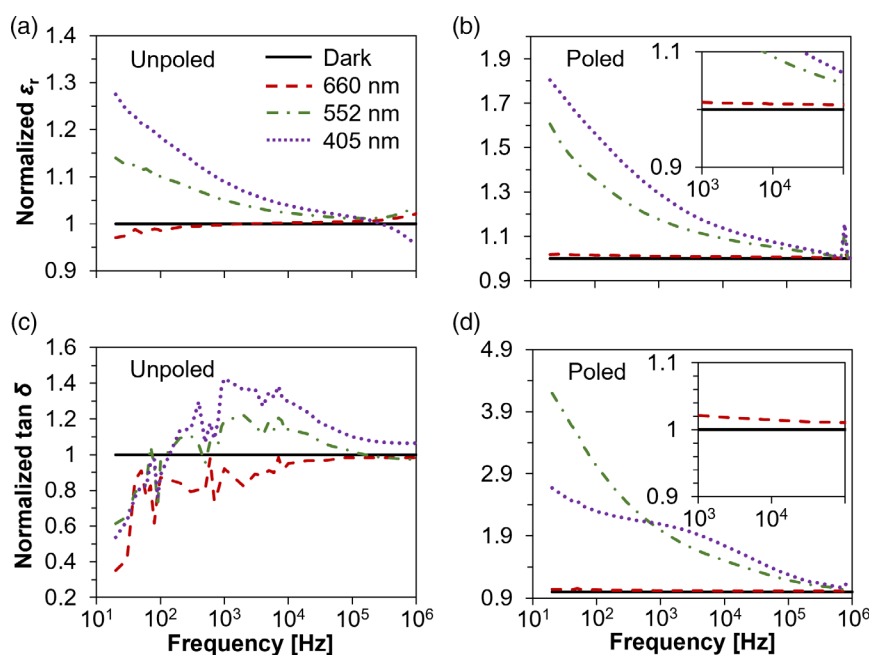


Figure 2. Dependence of a,b) normalized measured relative permittivity (ϵ_r) and c,d) normalized dielectric loss factor ($\tan \delta$) on measurement frequency for a,c) unpoled and b,d) poled KNBNNO sample in the dark and under different illuminations. The values obtained in the dark are normalized to “1”.

(Figure 2b). This trend followed that of the $\tan \delta$ at >1 kHz (Figure 2d), implying that photogenerated charge carriers in the sample started to influence the measured dielectric properties. Here, the increase of ϵ_r was more likely induced by the drastic increase of the imaginary component rather than that of the real permittivity. According to Figure S1b, Supporting Information, which shows a linear increase of absorption at >2.2 eV, as well as Figure 1a which identifies a direct bandgap of 2.12 eV, it is reasonable that the largest concentration of charge carriers was generated under the 405 nm light (3.06 eV) followed by the second largest while still substantial under the 552 nm light (2.25 eV). The minor increase under the 660 nm light (1.88 eV) could result from the contribution of in-gap states.^[17,43,44] Though the $\tan \delta$ values for 552 nm were larger than those for 405 nm at <1 kHz (Figure 2d), the conclusion of the ϵ_r change being dominated by $\tan \delta$ is considered generally true because both the values for 552 and 405 nm still showed a drastic increase compared to the dark level. The reversed relative positions at <1 kHz could be caused by stronger domain contribution to the ϵ_r for 405 nm at lower frequencies.^[15,26]

In Figure S3, Supporting Information, the absolute ϵ_r values measured in the dark were consistent to previous work, showing the replicability of the samples.^[14] The absolute $\tan \delta$ values measured in the dark doubled those in previous work, for example, ≈ 0.2 compared to <0.1 at 1 kHz.^[14] This was believed to be caused by the ITO electrode which possessed 1–2 k Ω resistance, while in previous work Pt electrode with negligible resistance was utilized.

In this work, the following photodetection should rely on the effect of photogenerated charge carriers to guarantee the reliability and replicability of the measurements by decreasing the chaos inside the material caused by photoexcited/stimulated domain

switching. Therefore, poled samples proceeded to the study of photodetection.

4. Photodetection

Figure S1c, Supporting Information, shows the microstructure of the perovskite–tungsten bronze interface area observed from the sample. Each larger grain ($\approx 1 \mu\text{m}$) consisted of multiple smaller grains (≈ 200 nm) as marked in the top subfigure and domain walls could be clearly seen in each smaller gain (marked in the bottom subfigure). Such a special microstructure resulted in the competition and frustration of the two polar phases forming simultaneously (orthorhombic perovskite and tetragonal polar tungsten bronze, see Table 1 and Figure S1a, Supporting Information), that is, the pseudo-MPB, as has been studied in previous works.^[18] Thanks to the large number of micrograins and domain walls, excellent ferroelectricity with a spontaneous polarization of $\approx 25 \mu\text{C cm}^{-2}$, remanent polarization of $\approx 20 \mu\text{C cm}^{-2}$, and coercive field of $\approx 1.5 \text{ kV mm}^{-1}$ was achieved, as shown in Figure S1d, Supporting Information. The strong ferroelectricity which is comparable to that of the conventional, wide-bandgap counterparts (e.g., (K,Na)NbO₃, BaTiO₃, PZT (Pb(Zr,Ti)O₃)), in addition to the narrow bandgap (≈ 2 eV in contrast to >3 eV for conventional counterparts), makes the KNBNNO in this work a unique candidate when using the cumulative optical and electrical stimuli for photodetection.^[13,17,45]

Figure 3a shows the schematic of the measurement configuration for conductivity under illumination and photodetecting performance of the KNBNNO ceramic sample. The ITO-coated sample was placed on a conductive substrate and the terminals of the source meter were effectively probed in both the sample surfaces where ohmic contact between the probes and ITO electrodes was guaranteed. Figure 3b shows the J – E (current

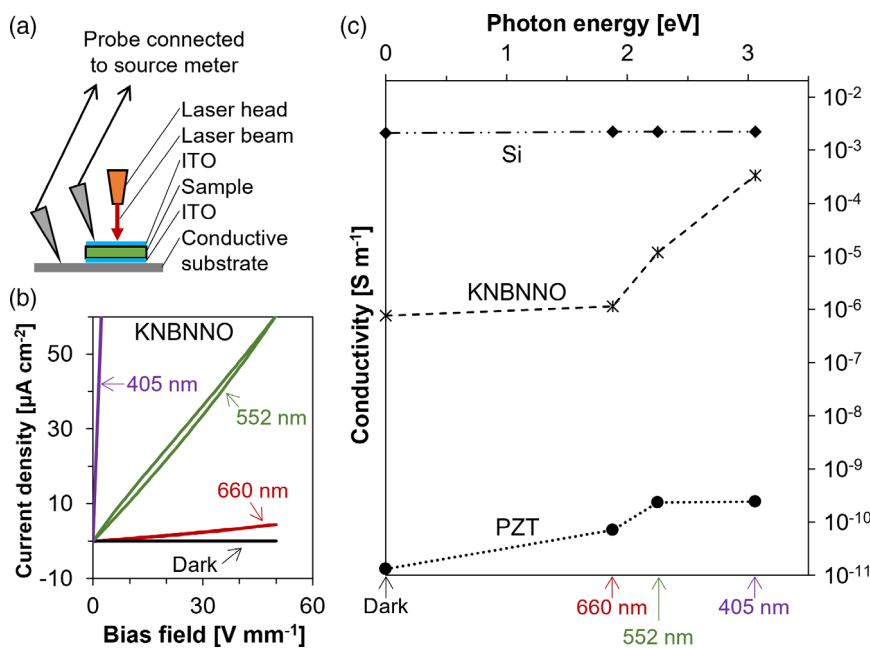


Figure 3. a) Schematic of the measurement configuration. b) Dependence of current density on bias electric field in the dark and under different illuminations for KNBNNO. c) Dependence of conductivity on incident photon energy for Si, KNBNNO, and PZT samples.

density–electric field) curves measured in the dark and under illuminations with different wavelengths. The output power of the lasers was set to be always 20 mW and the sample was irradiated for 10 min before starting each measurement. The correspondingly calculated conductivity values, together with those of the reference Si and PZT samples, are shown in Figure 3c.

The KNBNNO sample was a good insulator in the dark given the 10^{-6} S m^{-1} level dark conductivity (Figure 3b,c), as well as the standard, nonlossy ferroelectric hysteresis loop (Figure S1d, Supporting Information). The photon energy of the 660 nm illumination (1.88 eV) was likely to be under the bandgap, resulting in only a slight increase of the conductivity probably due to absorption of topological defects (e.g., domain walls or grain boundaries) which might have a lower bandgap than the bulk of the material.^[46] Those of the 552 nm (2.25 eV) and 405 nm (3.06 eV) illuminations were undoubtedly above the bandgap with the phenomenon of light-induced charge carriers, contributing to the output currents and thus a drastic increase of conductivity. Indeed, as the dipole-transition

photoabsorption dominated the excitation spectra, the electrons from valance band were thus photoexcited to the conduction band.^[47] The excitonic spectrum in Figure 1d denoted the electron's existence in the conduction band after photoexcitation with wavelengths of $<420 \text{ nm}$ (referring to the first absorption peak at 410 nm). Moreover, the slow components in Figure 1c, as a typical signature of electron migration, allowed charge transfer between adjacent phases, as shown in Figure S1 and S2, Supporting Information. The entire KNBNNO sample then became conductive once a bias field was imposed. These factors resulted in obvious current density and conductivity increases. It is worth noting that the sample might be partially conductive under irradiance of light when the photon energy was above the bandgap energy. Therein, the photoexcitation of electrons from the valance band might occur through, for example, electric quadrupole scheme or with assistance of phonons. As a result, a reduced conductivity was obtained. The sharp edge at $\approx 2 \text{ eV}$ in Figure 3c reinforces the earlier determination of the bandgap (Section 2). The conductivity difference spanned over three orders of magnitudes for KNBNNO (Figure 3c).

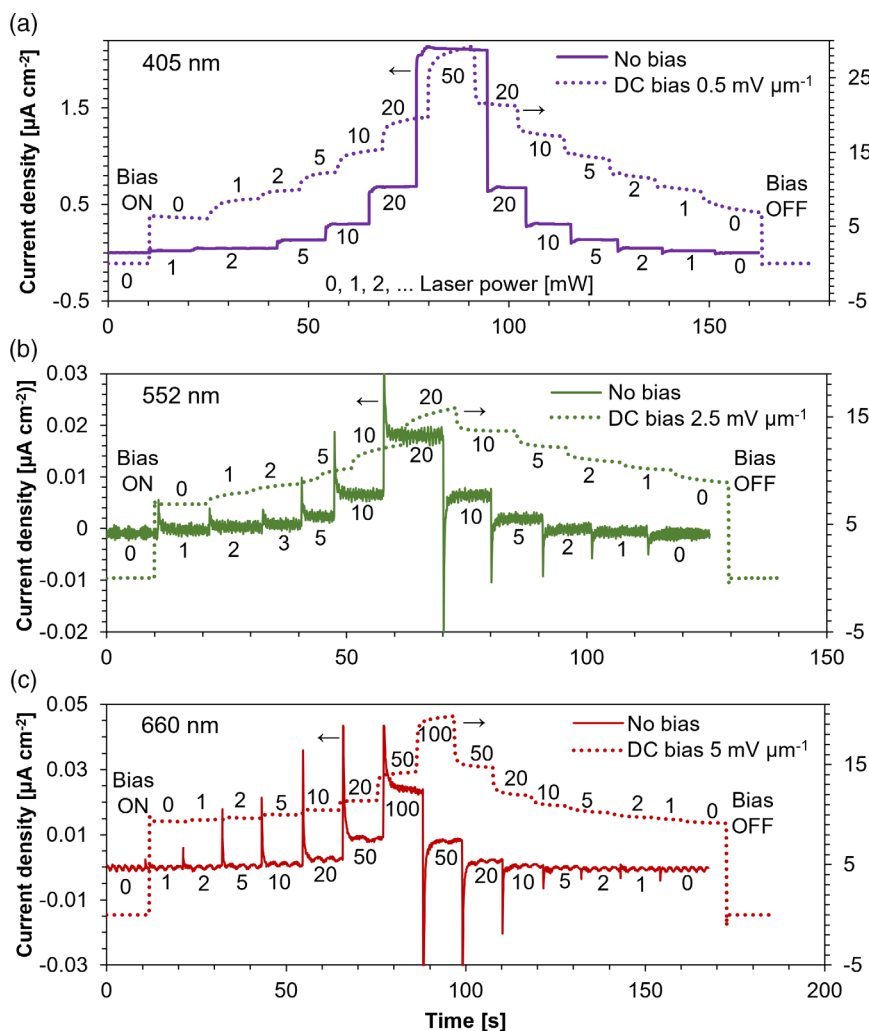


Figure 4. Evolution of current density in time for the KNBNNO photodetector measured under different lighting conditions: a) 405 nm, b) 552 nm, and c) 660 nm, as well as under different external bias electric fields. The numbers labeled next to the data plots indicate the laser power.

Figure S4, Supporting Information, provides the original $J-E$ curves which were used for conductivity calculation in Figure 3c measured from the Si and PZT references. In comparison, although the Si showed three orders of magnitude higher dark conductivity than KNBNNO, the change of conductivity under different illuminations was negligible, implying poor selectivity of incident light wavelength (Figure S4a, Supporting Information, Figure 3c). The PZT had a wide bandgap (>3 eV) but the below-gap incident photon energies in Figure 3c increased the conductivity from the dark condition to some extent. However, the overall conductivity values are too small to allow reliable current measurement ($<nA\text{ cm}^{-2}$ level, Figure S4b, Supporting Information) in practice. The PZT also showed particularly poor selectivity between the 405 and 552 nm light (Figure 3c). Therefore, the KNBNNO's vast variation of conductivities when subject to different incident photon energies was the ground for filterless, wavelength-selective photodetection/color sensing in this work.

The photodetecting behavior is illustrated in Figure 4 by comparing the output current density measured with different wavelengths and intensities of the incident lights as well as under different bias electric fields. Under certain DC bias, the device exhibited clear sensitivity to incident light intensity within the same wavelength. In order to tell the wavelength being detected without knowing it beforehand, one needs to compare the difference of current density between the zero-bias condition and that

under different bias fields. Figure 5a visualizes the mechanism of the wavelength selection, where Δ represents how many orders of magnitude the current density increased by from the values under zero electric bias to certain bias. The procedures for simultaneous blind wavelength and intensity determinations can be as follows, for example: 1) measure current density without electric bias and 2) measure current density under $0.5\text{ mV }\mu\text{m}^{-1}$ bias. If the current density increased by at least one order of magnitude, the wavelength should be similar to 405 nm. 3) Measure current density under $0.5\text{ mV }\mu\text{m}^{-1}$ bias. If the current density increased by at least two orders of magnitude, continue to measure under $2.5\text{ mV }\mu\text{m}^{-1}$ bias. If the increase went up to almost 3–4 orders of magnitude, the wavelength should be similar to 552 nm. 4) If the nearly 3–4 orders of magnitude increase was achieved by applying $5\text{ mV }\mu\text{m}^{-1}$ bias, the wavelength should be similar to 660 nm. 5) The measured current density and the illumination/dark ratio can then be compared and fit to Figure 5b,c, respectively, to figure out the intensity (incident power density).

It is admitted that the current device is yet to be a perfect model for complete and comprehensive mapping of the wavelengths and intensities of incident lights. As can be realized in Figure 5, only when the wavelength difference was large enough, for example, >100 nm, could the wavelength selection become effective. There are several steps ahead toward using such a mechanism to truly tell the wavelength blindly, including

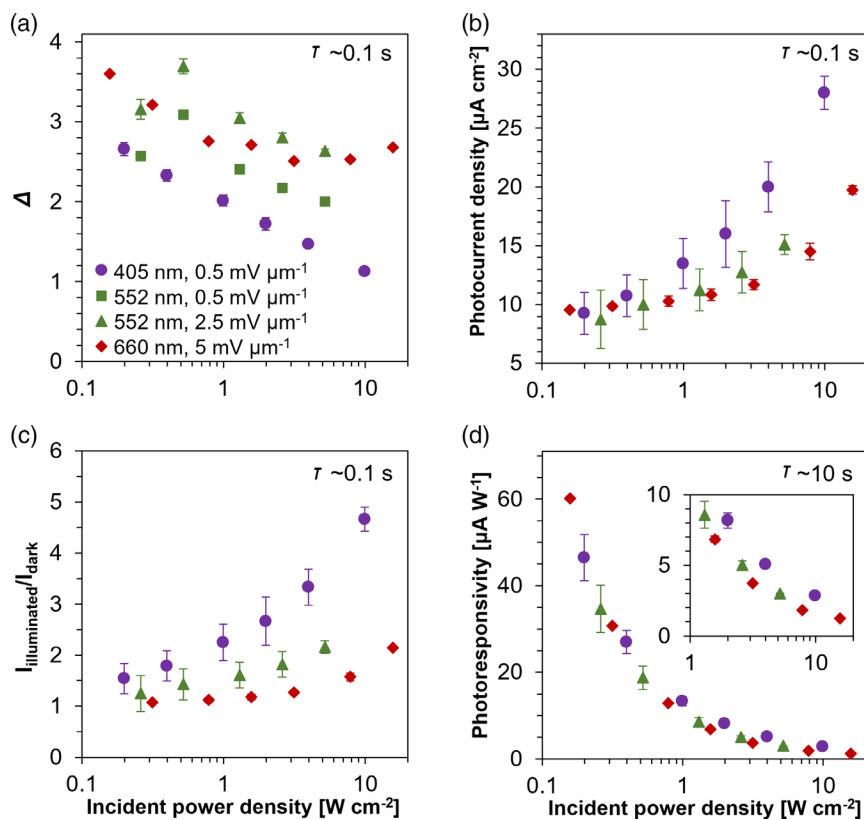


Figure 5. Dependence of a) Δ , logarithmic difference between the current densities under certain electric bias and under zero bias, b) photocurrent density under bias, c) ratio of the photocurrent density-to-dark current density under bias, and d) photoresponsivity under bias, on power density of the incident light. τ indicates the response time.

Table 2. Comparison of different photodetectors.

Material	Wavelength [nm]	Bias [V]	Responsivity [A W^{-1}]	EQE [%]	Dark current	Rise time	Decay time	Reference
Graphene	1550	0.4	6.1×10^{-3}	–	$\approx 200 \mu\text{A}$	–	–	[7]
Monolayer MoS_2	400–680 (non-selective)	8	880 (@561 nm)	–	2 pA	4 s	9 s	[8]
Vertically stacked organic semiconductors	455 and 528 (selective)	3	0.06–0.1	≈ 15	–	$< 70 \mu\text{s}$	–	[10]
$\text{K}_2\text{Nb}_8\text{O}_{21}$ nanowire	320	5	2.53	9.82	1.2 pA	$< 0.3 \text{ s}$	$< 0.3 \text{ s}$	[49]
KNb_3O_8 nanobelt	254	0–5	30	–	7.1 fA	2.5	1.8	[50]
Ba-/Ni-codoped (K,Na) NbO_3 ferroelectric ceramic	405, 552 and 660 (selective)	0.25–2.5	up to 6×10^{-5}	up to 0.1	pA level	0.1 s	10 s	This work

making thin films that boost the current density to improve selectivity and optimizing the device structure to increase the stability of current output and hence the accuracy of intensity measurement. However, it should be noted that this work is the first of its kind to demonstrate a potentially alternative concept for photodetection using ferroelectric materials. The data reported in this work may act as a baseline for improvements.

Nevertheless, according to Figure 5a–c, larger incident power densities tended to result in even better selectivity of both wavelength and intensity. This was partly because the sample was rather thick for a relatively short response time ($\approx 0.1 \text{ s}$) as photoferroelectric ceramics need time to reach an equilibrium of charge carrier flow upon being exposed to incident light.^[48] Reducing the sample thickness or elongating the response time will improve the selectivity and accuracy for smaller incident power densities. Figure 5d proves that similar photoresponsivities can be reached for all the studied wavelengths, providing reliable and comparable photodetection results even across different wavelengths if sufficiently long response time ($\approx 10 \text{ s}$) is allowed. Again, reducing the device thickness will help to reduce the saturation response time.

Figure S5, Supporting Information, shows the spectral photoresponsivity (R_i) and external quantum efficiency (EQE) of KNBNNO ceramics measured from the configuration shown in Figure 3a. The results are compared in Table 2 with relevant works reported in literature. It can be seen that the major advantage of using KNBNNO ferroelectric ceramics could be the monolithic structure to achieve wavelength selectivity that would have required a stacked structure made from different compounds.^[10] Considering the extremely large dimension between the electrodes (500–600 μm) in this work compared to the counterpart nanomaterials, the dark current and response time of the KNBNNO detector look competitive.^[8,49,50] Under a bias voltage similar to those in other works (Table 2), the KNBNNO detector exhibited rather small responsivity and EQE. This is partially because of the measurement and device configurations. The planar dimensions of the samples were roughly at $\text{cm} \times \text{cm}$ level which were fully covered by electrodes while the spot sizes of the incident laser beams were maximum 800 μm . The illuminated area was negligible compared to the electrically connected area, distorting the ratios of illuminated current and dark current and leading to an unfair calculation and thus assessment of the EQE and responsivity. This brings an interesting future

research topic of fabricating nanoscale KNBNNO devices and re-evaluating the optoelectrical properties with a fair comparison with counterparts.

5. Conclusion

This work for the first time has demonstrated the use of bandgap-engineered photoferroelectric ceramic, Ba- and Ni-codoped (K,Na) NbO_3 , for filterless and wavelength-selective photodetection. The intentionally designed A-site vacancy, that is, deficiency of K and/or Na in the initial raw material mixture, determines the phase formation, which is crucial for both optimization of ferroelectric properties and tuning of bandgap. Proper doping of such a composition by Ni and Ba lowers the band–band transition. The ceramic has obtained a direct bandgap of $\approx 2 \text{ eV}$ and a spontaneous polarization of $\approx 0.25 \text{ C m}^{-2}$. Simultaneous determination of wavelength and intensity has been realized via comparing zero-bias and biased photocurrents. Thus, the current density under $0.5 \text{ mV } \mu\text{m}^{-1}$ bias and 405 nm illumination increased by one order of magnitude while for 552 nm with the same bias the increase has been two orders of magnitude. By applying $5 \text{ mV } \mu\text{m}^{-1}$ bias, 3–4 orders of magnitude increase of the current density has been achieved for 660 nm illumination. Further comparison of the measured current density and the illumination/dark ratio to the calibrated results has allowed to figure out the intensity (incident power density). Despite the smaller photoresponsivity of $60 \mu\text{A W}^{-1}$ than those of classic photodetectors, the concept in this work offers an energy-efficient design (due to the small electric bias) and simple, cost-effective device configuration (plate capacitor made from ceramic samples via solid-state reaction) for filterless color sensing. Improvements can be made to extend the detectable wavelength range by further bandgap engineering and to reduce the response time/increase the photoresponsivity by fabricating thin-film devices.

6. Experimental Section

Fabrication of Materials: Ceramic samples were made via the solid-state reaction. The nominal composition of the raw powder was $(\text{K}_{0.45} \pm 0.01 \text{Na}_{0.37} \pm 0.02 \text{Ba}_{0.05} \pm 0.005) (\text{Nb}_{0.98} \pm 0.001 \text{Ni}_{0.02} \pm 0.001) \text{O}_{2.93} \pm 0.01$ from the stoichiometry of the starting reactants of K_2CO_3 ($\geq 99\%$, J.T. Baker, USA), Na_2CO_3 ($\geq 99\%$, Sigma-Aldrich, USA), BaCO_3 (99.98%, Aldrich Chemistry, USA), Nb_2O_5 (99.9%, Aldrich Chemistry, USA), and NiO

(99.999%, Aldrich Chemistry, USA). The nominal composition was characterized by X-ray fluorescence (XRF) (ASX S4 Pioneer, Bruker, USA). The reactants were weighed precisely, mixed on a ball-milling machine in a ZrO₂ jar filled with 3 mm ZrO₂ milling beads and ethanol, dried in oven at 80 °C, and then calcined at 825 °C. The calcined powder was ball milled again and the dried powder was formed into green bodies under uniaxial pressure of 90 MPa. The subsequent sintering was carried out at 1150 °C in air. Identified by XRD (D8 Discover, Bruker, USA) and electron probe microanalyzer (EPMA) (JXA-8530Fplus, JEOL, Japan), the sintered ceramics contained 83 ± 8 mol.% perovskite phase with a nominal chemical formula of (K_{0.54} ± 0.02Na_{0.37} ± 0.02Ba_{0.03} ± 0.005)(Nb_{0.996} ± 0.001Ni_{0.004} ± 0.001)O_{2.98} ± 0.01 and 17 ± 8 mol.% tungsten bronze phase with a nominal chemical formula of (K_{0.25} ± 0.02Na_{0.10} ± 0.01Ba_{0.19} ± 0.01)(Nb_{0.97} ± 0.005Ni_{0.03} ± 0.005)O_{2.82} ± 0.01, as has been summarized in Table 1. The compositional designs and studies are detailed in previous works.^[14,18,19]

Material Characterization: Some sintered ceramics were crushed in a mortar and then measured under XRD for phase identification. The complete ceramic samples were polished to the thickness of 500–600 μm with P1200 silicon carbide abrasive paper and then a polishing plate and diamond suspension (grain size 1 μm, MD-Nap and DiaPro, respectively, Struers, USA) to achieve a surface roughness of 50–60 nm. The polished samples were characterized in a UV–vis–NIR spectrophotometer (Cary 500 Scan, Varian, USA) to obtain optical properties. They were also coated with carbon and observed under field-emission scanning electron microscope (FESEM) Sigma, Zeiss, Germany) for the microstructure. The samples were then further polished to a surface roughness of ≈5 nm using a 250 nm grain-sized diamond suspension (DiaPro Nap 1/4, Struers, USA), followed by AFM analysis (Nanosurf, FlexAFM, UK) in the contact mode (10 mm × 10 mm) to observe the surface morphology. The above characterizations were carried out at room temperature.

In addition, PL spectroscopy was carried out on the polished samples. Time-resolved luminescence spectra were obtained upon excitation by wavelength-tunable pulsed solid-state laser (210–2300 nm, NT342/3UV, Ekspla, Lithuania). The emission signal was detected by the charge-coupled device (CCD) camera (iSTAR DH734-18 mm, Andor Technology, UK) coupled to the spectrometer (SR-303i-B, Andor Technologies, UK). Luminescence decay kinetics were measured by a photomultiplier tube PG122 with a time resolution better than 5 ns and a digital oscilloscope (TDS684A, Tektronix, USA). The samples were placed on the cold finger of the close cycle cryostat (ARS DE-204PB cryohead and ARS-4HW compressor, Advanced Research Systems, USA). The excitation spectra were measured with the FLS1000 spectrometer (Edinburgh Instruments, UK).

Electrical Characterization: The polished samples for electrical measurements were coated with 200 nm-thick transparent ITO (indium tin oxide) electrodes via sputtering on both surfaces. An inductor-capacitor-resistor (LCR) meter (E4980AL, Keysight, USA) and a source meter (Model 2450, Keithley, USA) were used to obtain the photodielectric properties and the *J*–*E* curves, respectively. Monochromatic lasers (OBIS LX/LS series, Coherent, USA) with wavelengths of 405, 552, and 660 nm were used as the light sources. For photodetection, current densities as a function of time were collected using the source meter in the dark and under illumination with different DC bias electric fields being present. The ferroelectric properties were evaluated by the Precision LCII system (Radiant Technologies, USA). As references, a piece of commercial p-type silicon wafer (Okmetic, Finland) and a commercial PZT (Pb(Zr,Ti)O₃)-5A piezoelectric/ferroelectric ceramic disc (Piezo.com, USA) were also measured with the source meter using the same sample configuration. All the electrical characterizations were conducted at room temperature. Poling was carried out in the dark where applicable by immersing the sample in room-temperature silicone oil while applying an external DC electric field of 3 kV mm⁻¹ for 10 min. The oil was cleaned in ethanol after poling and before measurement.

Supporting Information

Supporting Information is available from the Wiley Online Library or from the author.

Acknowledgements

This work was supported by University of Oulu and the European Research Council (ERC) under the ERC Starting Grant (agreement number 101039110). V.B. acknowledges the EDUFI Fellowship provided by the Finnish National Agency for Education. F.T. and W.C. acknowledge financial support from the European Research Council (ERC) under the European Union's Horizon 2020 research and innovation programme (grant agreement no. 101002219). The Institute of Solid State Physics, University of Latvia as the Center of Excellence, has received funding from the European Union's Horizon 2020 Framework Programme H2020-WIDESPREAD-01-2016-2017-TeamingPhase2 under grant agreement no. 739508, project CAMART2.

Conflict of Interest

The authors declare no conflict of interest.

Author Contributions

Y.B. worked on the idea and coordination. V.B., F.T., V.P., and Y.B. conducted experiments. Y.B. and W.C. took care of data interpretation. V.B. and F.T. contributed equally to this work. All authors collaboratively wrote the paper.

Data Availability Statement

The data that support the findings of this study are available from the corresponding author upon reasonable request.

Keywords

KNBNNO, perovskites, photodielectrics, photoferroelectrics, photoluminescence, photosensors

Received: November 2, 2022

Revised: November 20, 2022

Published online: November 30, 2022

- [1] E. R. Fossum, *IEEE Trans. Electron Devices* **1997**, *44*, 1689.
- [2] S. Li, A. Pandharipande, F. M. J. Willems, *IEEE Sens. J.* **2016**, *16*, 3216.
- [3] P. H. Pathak, X. Feng, P. Hu, P. Mohapatra, *IEEE Commun. Surv. Tutor.* **2015**, *17*, 2047.
- [4] S. Li, Y. Zhang, W. Yang, H. Liu, X. Fang, *Adv. Mater.* **2020**, *32*, 1905443.
- [5] X. Fang, L. Hu, K. Huo, B. Gao, L. Zhao, M. Liao, P. K. Chu, Y. Bando, D. Golberg, *Adv. Funct. Mater.* **2011**, *21*, 3907.
- [6] Q. Chen, D. Chitnis, K. Walls, T. D. Drysdale, S. Collins, D. R. S. Cumming, *IEEE Photon. Technol. Lett.* **2012**, *24*, 197.
- [7] T. Mueller, F. Xia, P. Avouris, *Nat. Photon.* **2010**, *4*, 297.
- [8] O. Lopez-Sanchez, D. Lembke, M. Kayci, A. Radenovic, A. Kis, *Nat. Nanotechnol.* **2013**, *8*, 497.
- [9] F. P. García de Arquer, A. Armin, P. Meredith, E. H. Sargent, *Nat. Rev. Mater.* **2017**, *2*, 16100.
- [10] T. Zhao, K. Xia, D. Natali, V. Pecunia, *Adv. Opt. Mater.* **2022**, *10*, 2200862.
- [11] P. Lopez-Varo, L. Bertoluzzi, J. Bisquert, M. Alexe, M. Coll, J. Huang, J. A. Jimenez-Tejada, T. Kirchartz, R. Nechache, F. Rosei, Y. Yuan, *Phys. Rep.* **2016**, *653*, 1.

- [12] C. Paillard, X. Bai, I. C. Infante, M. Guennou, G. Geneste, M. Alexe, J. Kreisel, B. Dkhil, *Adv. Mater.* **2016**, *28*, 5153.
- [13] G. Vats, J. Peräntie, J. Palosaari, J. Juuti, J. Seidel, Y. Bai, *ACS Appl. Electron. Mater.* **2020**, *2*, 2829.
- [14] Y. Bai, C. Prucker, N. H. Khansur, *J. Am. Ceramic Soc.* **2022**, *105*, 3364.
- [15] Y. Bai, G. Vats, J. Seidel, H. Jantunen, J. Juuti, *Adv. Mater.* **2018**, *30*, 1803821.
- [16] Y. Bai, H. Jantunen, J. Juuti, *Adv. Mater.* **2018**, *30*, 1707271.
- [17] Y. Bai, H. Jantunen, J. Juuti, *ChemSusChem* **2019**, *12*, 2540.
- [18] Y. Bai, A. A. Kistanov, W. Cao, J. Juuti, *J. Phys. Chem. C* **2021**, *125*, 8890.
- [19] Y. Bai, *Open Ceram.* **2021**, *5*, 100079.
- [20] Y. Bai, H. Xiang, H. Jantunen, J. Juuti, *Eur. Phys. J. Spec. Top.* **2019**, *228*, 1555.
- [21] Y. Bai, J. Palosaari, P. Tofel, J. Juuti, *Energy Technol.* **2020**, *8*, 2000461.
- [22] B. Ducharne, J. Juuti, Y. Bai, *Adv. Theory Simul.* **2020**, *3*, 2000052.
- [23] G. Vats, Y. Bai, J. Seidel, *Adv. Photon. Res.* **2021**, *2*, 2100050.
- [24] G. Vats, J. Peräntie, J. Juuti, J. Seidel, Y. Bai, *Energy Technol.* **2020**, *8*, 2000500.
- [25] Y. Bai, P. Tofel, J. Palosaari, H. Jantunen, J. Juuti, *Adv. Mater.* **2017**, *29*, 1700767.
- [26] G. Vats, Y. Bai, D. Zhang, J. Juuti, J. Seidel, *Adv. Opt. Mater.* **2019**, *7*, 1800858.
- [27] V. A. Balanov, Z. Zhao, M. Pan, A. Feldhoff, Y. Bai, *J. Solgel. Sci. Technol.* **2020**, *96*, 649.
- [28] S. Ithurria, M. D. Tessier, B. Mahler, R. P. S. M. Lobo, B. Dubertret, Al. L. Efros, *Nat. Mater.* **2011**, *10*, 936.
- [29] A. C. Arsenault, T. J. Clark, G. von Freymann, L. Cademartiri, R. Sapienza, J. Bertolotti, E. Vekris, S. Wong, V. Kitaev, I. Manners, R. Z. Wang, S. John, D. Wiersma, G. A. Ozin, *Nat. Mater.* **2006**, *5*, 179.
- [30] B. Monemar, P. P. Paskov, G. Pozina, C. Hemmingsson, J. P. Bergman, T. Kawashima, H. Amano, I. Akasaki, T. Paskova, S. Figge, D. Hommel, A. Usui, *Phys. Rev. Lett.* **2009**, *102*, 235501.
- [31] S. Godefroo, M. Hayne, M. Jivanescu, A. Stesmans, M. Zacharias, O. I. Lebedev, G. van Tendeloo, V. v. Moshchalkov, *Nat. Nanotechnol.* **2008**, *3*, 174.
- [32] P. Talebi, A. A. Kistanov, E. Rani, H. Singh, V. Pankratov, V. Pankratova, G. King, M. Huttula, W. Cao, *Appl. Energy* **2022**, *322*, 119461.
- [33] S. Flessau, C. Wolter, E. Pösel, E. Kröger, A. Mews, T. Kipp, *Phys. Chem. Chem. Phys.* **2014**, *16*, 10444.
- [34] M. Sotoodeh, A. H. Khalid, A. A. Rezazadeh, *J. Appl. Phys.* **2000**, *87*, 2890.
- [35] P. P. Paskov, P. O. Holtz, B. Monemar, J. M. Garcia, W. V. Schoenfeld, P. M. Petroff, *Appl. Phys. Lett.* **2000**, *77*, 812.
- [36] W. Du, S. A. Ghetmiri, B. R. Conley, A. Mosleh, A. Nazzal, R. A. Soref, G. Sun, J. Tolle, J. Margetis, H. A. Naseem, S.-Q. Yu, *Appl. Phys. Lett.* **2014**, *105*, 51104.
- [37] H. Li, X. H. Zhang, *Opt. Mater.* **2020**, *107*, 110150.
- [38] D. J. Robbins, P. J. Dean, *Adv. Phys.* **1978**, *27*, 499.
- [39] J. Wang, J. Wang, N. Li, X. Du, J. Ma, C. He, Z. Li, *ACS Appl. Mater. Interfaces* **2020**, *12*, 31477.
- [40] J. R. Lakowicz, Ed., in *Principles of Fluorescence Spectroscopy*, Springer, New York, NY, **2006**, pp. 1–60.
- [41] F. Rubio-Marcos, D. A. Ochoa, A. del Campo, M. A. García, G. R. Castro, J. F. Fernández, J. E. García, *Nat. Photon.* **2018**, *12*, 29.
- [42] F. Rubio-Marcos, A. del Campo, J. Ordoñez-Pimentel, M. Venet, R. E. Rojas-Hernandez, D. Páez-Margarit, D. A. Ochoa, J. F. Fernández, J. E. García, *ACS Appl. Mater. Interfaces* **2021**, *13*, 20858.
- [43] H. Xiao, W. Dong, Y. Guo, Y. Wang, H. Zhong, Q. Li, M.-M. Yang, *Adv. Mater.* **2019**, *31*, 1805802.
- [44] H. Zhong, H. Xiao, N. Jiao, Y. Guo, *J. Am. Ceram. Soc.* **2019**, *102*, 6422.
- [45] T. Zheng, J. Wu, D. Xiao, J. Zhu, *Prog. Mater. Sci.* **2018**, *98*, 552.
- [46] J. Seidel, D. Fu, S.-Y. Yang, E. Alarcón-Lladó, J. Wu, R. Ramesh, J. W. Ager, *Phys. Rev. Lett.* **2011**, *107*, 126805.
- [47] V. Pankratov, J. Hozzowska, J.-C. Dousse, M. Huttula, A. Kis, D. Krasnozhan, M. Zhang, W. Cao, *J. Phys. Condens. Matter* **2015**, *28*, 15301.
- [48] L. Wu, A. M. Burger, A. L. Bennett-Jackson, J. E. Spanier, P. K. Davies, *Adv. Electron. Mater.* **2021**, *7*, 2100144.
- [49] H. Liu, Z. Zhang, L. Hu, N. Gao, L. Sang, M. Liao, R. Ma, F. Xu, X. Fang, *Adv. Opt. Mater.* **2014**, *2*, 771.
- [50] Y. Ping, H. Long, H. Liu, C. Chen, N. Zhang, H. Jing, J. Lu, Y. Zhao, Z. Yang, W. Li, F. Ma, X. Fang, Z. Wei, H. Xu, *Adv. Funct. Mater.* **2022**, *32*, 2111673.